

# Broadband Microelectromechanical Systems-Based Silicon Nitride Photonic Switch

Shubhashree Swain,\* Michal Zawiarta, Jega Gurusamy, Mariusz Martyniuk, Adrian Keating, Gino Putrino, Lorenzo Faraone, and Dilusha Silva

Over the past three decades, silicon photonic devices have been core to the realization of large-scale photonic-integrated circuits. However, silicon nitride is another key complementary metal oxide semiconductor-compatible material for high-density photonic-integrated circuits, having low manufacturing costs, low optical losses, and excellent mechanical properties, that can provide enhanced performance over silicon in an integrated photonic platform. This article presents the design, fabrication, and testing of a proof-of-concept switchable silicon nitride photonic coupler that leverages these properties combined with microelectromechanical systems actuation. The photonic platform uses a moveable suspended waveguide to enable efficient out-of-plane switching and is built using conventional lithographic techniques to demonstrate the high compatibility with existing microelectronic fabrication techniques. The photonic switch is measured to have an insertion loss of 2.6 dB and an ON/OFF extinction ratio of 34 dB at the output of the suspended waveguide, at a wavelength of 1470 nm. Detailed simulations demonstrate broadband operation over a 600 nm wavelength range from 1.25 to 1.85  $\mu\text{m}$  which is experimentally validated over the range from 1.25 to 1.61  $\mu\text{m}$ . To the best of knowledge, this is the broadest operation range ever demonstrated by a photonic switch in simulation.

(a few milliwatts to tens of milliwatts).<sup>[20–29]</sup>

This has increased the number of implementations of optical switches for a variety of applications related to telecommunication networks, high-performance computing, and quantum technologies.<sup>[30,31]</sup> Silicon waveguides have been widely used in photonic switches due to their ability to integrate with complementary metal oxide semiconductor manufacturing process technology, however, the high refractive index of silicon makes coupling to standard fiber difficult due to the extremely small optical mode field diameter.<sup>[32,33]</sup>

There have been several reports of Si photonic switches that employ various tuning mechanisms such as thermo-optic, plasma dispersion, electro-optic, and microelectromechanical systems (MEMS). In thermo-optic switches, waveguide coupling is modified by varying the refractive index of the material using (generally) an electrical heater.<sup>[28,32–34]</sup> Such a tuning mechanism offers low optical loss and a small footprint at the expense of high

## 1. Introduction

Over the past two decades, optical switches have shown immense promise for broad bandwidth (1.25–1.65  $\mu\text{m}$ )<sup>[1–5]</sup> along with low levels of input-to-output optical loss (from fractions of a dB to a few dB),<sup>[6–13]</sup> fast switching time (ranging from ns to sub- $\mu\text{s}$ ),<sup>[14–19]</sup> and relatively low power consumption per switch

power consumption and low switching speed due to the long thermal time constant.<sup>[35]</sup> By engineering the structures to improve thermal isolation, the power consumption has been considerably improved (sub-milliwatt) and the response time has been reduced to achieve sub-millisecond switching in these thermo-optic devices.<sup>[36,37]</sup> Faster switching can also be achieved using carrier injection or depletion of mobile charge carriers, through the process of plasma dispersion tuning of the refractive index.<sup>[38]</sup> Such electro-optic switches can generate a response time in nanoseconds. However, power consumption is generally high, around 7 mW/ $\pi$ , and has on-chip insertion loss of 3.7 dB  $\pm$  1.3 dB.<sup>[39]</sup> But inherently, in both thermo-optic and electro-optic switches, the coupling efficiency is low due to the small change in refractive index which can be achieved, demanding long waveguide lengths for mode-integration to occur. Alternatively, MEMS switching allows electromechanical actuation to modify the waveguide properties<sup>[18]</sup> which not only offers low power consumption and low optical loss but also supports the integration of a large number of switches in a small footprint (high density). Importantly, MEMS switching can provide significantly stronger optical interaction over a shorter length by physically moving the waveguide, which enables efficient, high-density switching between the waveguides.<sup>[40–43]</sup>


S. Swain, M. Zawiarta, J. Gurusamy, M. Martyniuk, A. Keating, G. Putrino, L. Faraone, D. Silva

ARC Centre of Excellence on Transformative Meta-Optical Systems (TMOS)

Department of Electrical, Electronic and Computer Engineering  
The University of Western Australia

Perth, Western Australia 6009, Australia

E-mail: shubhashree.swain@research.uwa.edu.au

 The ORCID identification number(s) for the author(s) of this article can be found under <https://doi.org/10.1002/adpr.202300213>.

© 2023 The Authors. Advanced Photonics Research published by Wiley-VCH GmbH. This is an open access article under the terms of the Creative Commons Attribution License, which permits use, distribution and reproduction in any medium, provided the original work is properly cited.

DOI: 10.1002/adpr.202300213

Many MEMS Si photonic switches have been reported in the literature that use directional couplers.<sup>[44,45]</sup> The actuation mechanisms of these switches use comb drives,<sup>[46]</sup> nanolatch mechanisms with comb drives,<sup>[47]</sup> or parallel plate actuators,<sup>[48]</sup> which consume low power and result in fast switching operation. However, the optical bandwidth of MEMS directional couplers has been limited to  $\approx 20$  nm.<sup>[44]</sup> To address this issue, a MEMS Si photonic switch comprising vertical adiabatic couplers has been demonstrated with low on-chip insertion loss (3.7 dB) and broadband operation (300 nm).<sup>[48]</sup> Thereafter, a monolithic Si photonic switch with fast switching time ( $< 1$   $\mu$ s) and broadband operation ( $> 120$  nm) have been reported.<sup>[49]</sup> However, the fabrication of these photonic switches requires high-resolution lithography tools such as deep-UV lithography. Apart from this, the discussed switching devices used Si as core waveguide material. Although Si has been widely used in photonic-integrated circuits, other materials such as silicon nitride offer comparable advantages, along with reduced optical loss due to moderate index contrast and the ability to operate across a wide range of frequencies.<sup>[20–22]</sup> However, only a few optical switches incorporating SiN<sub>x</sub> as the core waveguide material have been reported.<sup>[50–54]</sup> Considering the low optical loss and commercial availability of SiN<sub>x</sub> waveguides, we have chosen this as the core waveguide material for the designed MEMS adiabatic coupler.

In this work, a novel MEMS silicon nitride (SiN<sub>x</sub>) photonic switch has been designed, fabricated, and tested. These devices were fabricated at the Australia National Fabrication Facility-Western Australia node. The switch showed an insertion loss of 2.6 and 3.7 dB at wavelengths of 1470 and 1550 nm, respectively. The highest extinction ratio (ER) of 34 dB at the suspended waveguide was measured at 1470 nm. The switch has demonstrated broadband operation over a 600 nm wavelength range, which is the widest range reported by a MEMS photonic switch to date. Furthermore, the measured rise time was in the range of 10  $\mu$ s. To the best of our knowledge, this is the first report of a MEMS adiabatic photonic switch using SiN<sub>x</sub> waveguides and vertical parallel plate actuation.

## 2. Design Model

### 2.1. SiN<sub>x</sub> Photonic Switch

The operating principle of the SiN<sub>x</sub> photonic switch is presented in schematic form in **Figure 1a,b**. The coupler comprises a bottom waveguide (depicted in red) and a suspended top movable waveguide (shown in blue). In the OFF state, the waveguides are separated by a gap of 1.1  $\mu$ m, as depicted in **Figure 1a**, allowing unobstructed light propagation through the bottom waveguide toward the output. Upon activation of the switch (ON state), the suspended waveguide is electrostatically actuated toward the bottom waveguide, as illustrated in **Figure 1b**, allowing the coupling of light to the top suspended waveguide and directing it toward the top waveguide's output. The direction of light propagation is indicated by yellow arrows in **Figure 1a,b**.

The complete switch design, including the waveguide positions and actuation electrodes, is shown for both the OFF (**Figure 1c**) and ON (**Figure 1d**) states. The diagram highlights the placement of the bottom waveguide on the substrate, forming

a bend toward the output. The suspended membrane is made partially transparent for better visibility of the underlying layers in **Figure 1c,d**. The conducting connections associated with the actuation electrodes are not depicted in the figure for aesthetic reasons. The optical input and output locations for both the OFF and ON states are indicated by yellow arrows in the schematic. The suspended waveguide is positioned on a free-standing membrane which is anchored to the substrate on both sides of the waveguide along its length. Pairs of parallel actuator plates (electrodes shown in yellow in **Figure 1c,d**) facilitate electrostatic actuation, with one pair of actuator plates fixed to the substrate and another pair on the suspended membrane. When a voltage is applied between the top and bottom actuator plates, an electrostatic force is generated between them, attracting the top membrane along with the supported waveguide toward the underlying bottom waveguide. Both the anchors and actuator plates are placed sufficiently away from the waveguide to not interfere with the guided light and avoid inducing additional optical losses. A consistent gap between the waveguides is enforced using mechanical stoppers, for optimal evanescent coupling from the bottom waveguide to the suspended waveguide (the mechanical stoppers are not shown in the image).

The demonstrated switch consists of a bottom strip waveguide with SiN<sub>x</sub> as the core material, on a Si substrate, with an intermediate 4  $\mu$ m-thick SiO<sub>x</sub> layer. Air acts as the top cladding layer for the bottom waveguide. The bottom waveguide was designed for single-mode propagation at a wavelength of 1.55  $\mu$ m to have a constant width of 1.2  $\mu$ m (shown in **Figure 1a,b**) and a thickness of 450 nm. The suspended waveguide is supported by a 90 nm-thick SiN<sub>x</sub> suspended membrane which is depicted in **Figure 1c, d**. The suspended strip waveguide is composed of 450 nm thick SiN<sub>x</sub> as the core material and air as the top and bottom cladding layer. The width of the suspended waveguide is gradually tapered from 0.9 to 2  $\mu$ m (as indicated schematically in **Figure 1b**), with optical modeling confirming single-mode operation for a wavelength of 1.55  $\mu$ m up to a width of 1.5  $\mu$ m and transitioning to a multimode guiding for larger widths. The gradual tapering of the width of the suspended waveguide facilitates a gradual evolution of optical modes and enables adiabatic coupling of light. This approach effectively increases the tolerance of the design to fabrication imperfections compared to normal directional couplers.<sup>[44]</sup> When the device is turned ON, the “slope length” defined in **Figure 1f** on both the input and output of the suspended waveguide was measured to be 73  $\mu$ m in length, while the defined “contact length” was measured to be 32  $\mu$ m long. To better understand these lengths, imagine the suspended waveguide starting to slope downward from a certain point on both sides. This slope continues until it reaches a specific distance called the “contact length”, at that point, the suspended waveguide becomes parallel to the bottom waveguide. These dimensions for the switch design were selected to achieve the maximum coupling efficiency, as estimated by the optical simulations, taking into account the limitations of the conventional lithography process.

The suspended membrane of the main switching area has the dimensions of 146  $\mu$ m  $\times$  160  $\mu$ m and supports the top actuator plates. The top two actuation plates have dimensions of 38  $\mu$ m  $\times$  35  $\mu$ m each, to achieve the required contact length for efficient coupling of light between the bottom and the top waveguides. Silicon nitride is used as both waveguide's core

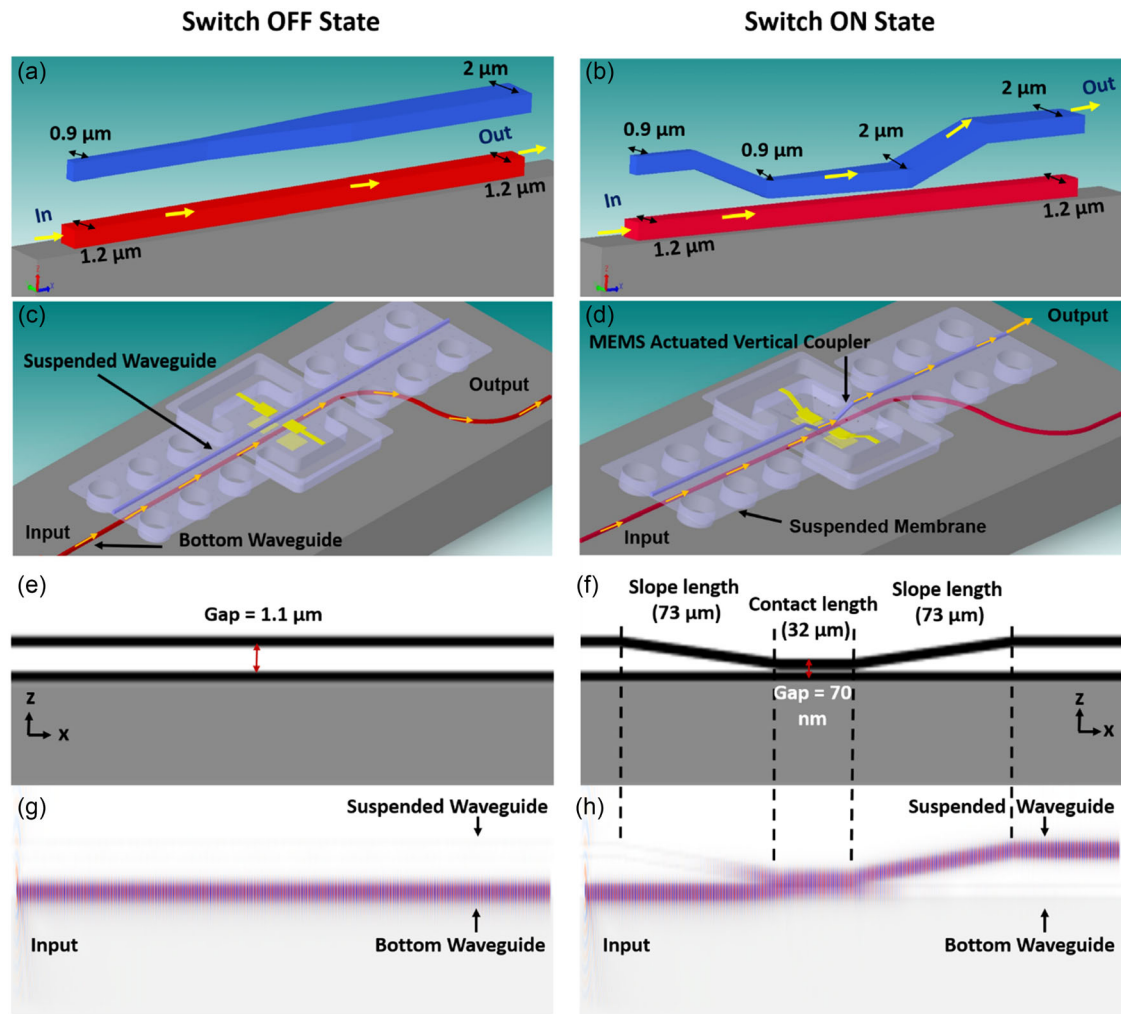


**Figure 1.** Representations of the MEMS SiN<sub>x</sub> photonic switch, featuring a bottom SiN<sub>x</sub> waveguide on a SiO<sub>2</sub>/Si substrate and a suspended SiN<sub>x</sub> waveguide, in two distinct states (OFF/ON). a) Schematic of the OFF state of the switch, b) the ON state of the switch, c,d) the 3D model of the designed switch, with arrows denoting the optical input and output directions for both the OFF (left) and ON (right) states. The FDTD simulations of the design (a) and (b) are displayed in e,g) and f,h), respectively, along the XZ-plane. The substrate is depicted in gray, and the two waveguides are shown in black. The gap between the waveguides is presented as (e) 1.1 μm in the OFF state, and (f) 70 nm in the ON state. The propagation of the field profiles is shown for the OFF state (g) and the ON state (h). The dotted lines in (f) indicate the nominal slope lengths (73 μm) and contact length (32 μm).

material as well as for the suspended membrane due to its excellent optical and mechanical properties. In addition, mechanical stoppers are incorporated in the design to maintain a 70 nm of gap between the two waveguides in the ON state of the switch. Their dimensions are designed to match the size of the bottom electrodes (40 μm × 38 μm). This aids in preventing potential device failures during the ON state, especially since the bottom waveguide of the device is not planarized. Electrostatic simulations were performed using CoventorWare software to determine the resonance frequency and required actuation voltages of the design. It was found that the device is predicted to resonate at a frequency of 801 KHz and require an actuation voltage of 52 V.

The advantages of this design over other existing adiabatic couplers include the low insertion loss and strong coupling efficiency generated between the two waveguides based on the adopted design and waveguide material selection. Existing

vertical adiabatic couplers<sup>[48,55,56]</sup> require the coupling waveguide to start abruptly to meet the adiabatic coupling condition. This necessitates the use of high-resolution lithography tools. In our design, by varying the approaching slope angle of the coupler waveguide, the coupling process commences before the start of the nominal contact length of the two waveguides (shown in Figure 1h). This approach assists in avoiding the necessity to have an abrupt start to the coupler waveguide. Apart from this, by using silicon nitride as the core waveguide material and for the suspended membrane, we have removed any issues associated with excessive compressive stress generated from SiO<sub>x</sub> leading to device failure (SiO<sub>x</sub> is commonly used as a cladding material for Si and SiN<sub>x</sub> waveguides in existing couplers). Residual stresses are known to be of significant importance for MEMS structures and have multiple points of origin, including defects present within the film.<sup>[57–59]</sup> Various studies in the

literature have previously reported on the residual stress of silicon nitride.<sup>[60–62]</sup> In the current design, it is desirable to achieve silicon nitride films with a slight tensile stress, as this results in flat MEMS structures which in our case while unactuated state were characterized to remain flat within 10 nm over the distance of 152 nm between the anchors. In the case of plasma-enhanced chemical vapour deposition (PE-CVD), this stress can be controlled by manipulating temperature, pressure, gas composition, power density, or RF frequency/power. The primary source of this stress in silicon nitride films is the strain within Si–N bonds. The stoichiometry of the silicon nitride has significant impact on the residual stress in the film. Optimizing deposition parameters for tensile films is a significant part of the MEMS fabrication process development.

## 2.2. Optical Simulation

The optical simulations of the switch have been performed using MEEP, an open-source finite difference time domain (FDTD) software. The waveguide structures were first created as a model within the simulation environment (as shown in Figure 1e,f), followed by a definition of the boundary conditions and optical launch conditions. The spatiotemporal evolution of the electromagnetic fields is then simulated, to examine the waveguide-to-waveguide coupling behavior under various configurations. Figure 1g,h illustrates the switching performance of the design, demonstrating the exclusive propagation of optical fields in the bottom waveguide when the device is switched OFF and the adiabatic coupling from the bottom to the suspended waveguide when it is switched ON.

To assess the optical field intensity, at the outputs of the on-substrate bottom waveguide and the suspended coupler waveguide, in both the OFF and ON states across a wide range of wavelengths (1.2–2  $\mu\text{m}$ ), numerical simulations are conducted. **Figure 2a** presents insertion loss (ignoring input and output coupling losses) as a function of wavelength, at the output of the suspended waveguide, when the coupler transitions from a 70 nm gap (ON state) to a 1.1  $\mu\text{m}$  gap (OFF state). Of interest is when the gap ranges from 70 to 200 nm, which demonstrates insertion loss below 2 dB for the wavelength range from 1.25 to 1.85  $\mu\text{m}$ . The value degrades for wavelengths longer than 1.85  $\mu\text{m}$ . As the gap increases from 200 nm to 1  $\mu\text{m}$ , insertion loss reaches 40 dB at a wavelength of 1.32  $\mu\text{m}$  and 27 dB at a wavelength of 1550 nm. The insertion losses are not constant across the entire wavelength range of 1.2–2  $\mu\text{m}$  for a 1  $\mu\text{m}$  gap between the waveguides.

Figure 2b depicts insertion loss, as a function of wavelength, for propagation paths exiting at either the bottom waveguide or the suspended waveguide, for the ON state of the switch. The bottom waveguide is represented in red, while the suspended waveguide is shown in blue. It can be observed that the insertion losses at the output of the suspended waveguide are 0.15 dB at 1550 nm and below 0.4 dB for the wavelength range of 1.2–1.85  $\mu\text{m}$ . The insertion losses for the suspended waveguide are more clearly illustrated in the zoomed-in inset (Figure 2b). The insertion loss at the output of the bottom waveguide is 27 dB at 1550 nm and ranges from 27 to 31 dB for wavelengths between 1.25 and 1.85  $\mu\text{m}$ . This confirms the broadband operation of the switch within the wavelength range of 1.25–1.85  $\mu\text{m}$

(600 nm range). As the gap between the waveguides increases, the transmission of light to the suspended waveguide decreases, as depicted in Figure 2a. At 1550 nm, the increase in gap from 70 nm to 1.1  $\mu\text{m}$ , reduced the insertion loss of the bottom waveguide from 32 to 0.07 dB (Figure 2c). Conversely, for the suspended waveguide, decreasing the spacing from 1.1  $\mu\text{m}$  to 70 nm results in a reduction in insertion loss from 27 to 0.15 dB. The ER, calculated as the ratio between the optical power transmitted in the ON state and the optical power transmitted in the OFF state, is expressed in dB scale. In this case, the ER at the output of both the bottom waveguide and suspended waveguide falls within 27–30 dB at 1550 nm (Figure 2c).

In Figure 2a,b, it is evident that for wavelengths longer than 1.9  $\mu\text{m}$  and irrespectively of the gap between the two waveguides, the insertion loss as measured at the output of the suspended waveguide is progressively more significant with increasing wavelength. This is due to the single mode cut-off in the bottom waveguide, with its current width of 1.2  $\mu\text{m}$  and thickness of 450 nm. As a result, light tends to leak into the bottom cladding, resulting in significant propagation loss in the bottom waveguide. This directly influences the light transmission into the suspended waveguide for wavelengths beyond 1.9  $\mu\text{m}$ , as shown in Figure 2d. The propagation of the field profiles for the ON state of the switch at wavelengths 2 and 2.5  $\mu\text{m}$  is shown in Figure 2e,f, respectively, and the field profiles at wavelength 1.55  $\mu\text{m}$  are presented in Figure 1h. In Figure 2e, a significant amount of light leaks into the bottom cladding, while the remaining light is transmitted into the suspended waveguide. However, in Figure 2f, the waveguide cannot support the modes at all, resulting in maximum leakage of light into the bottom cladding, resulting in virtually no light at the output of both waveguides. By expanding the width of the bottom waveguide from 1.2 to 2  $\mu\text{m}$ , it is possible to support single-mode operation up to a wavelength of 2.8  $\mu\text{m}$  with some multimode propagation at lower wavelengths.

For efficient switching of light from the bottom waveguide to the suspended waveguide, the effective alignment between both waveguides is crucial. To understand the effect of alignment offset between the waveguides, the insertion losses are calculated through optical simulations. This was done by adjusting the position of the suspended waveguide laterally up to 1  $\mu\text{m}$  away from the bottom waveguide. The predicted insertion loss is presented in **Figure 3** as a function of waveguide misalignment  $\delta$ , as depicted in the inset of Figure 3. The data presented in Figure 3 indicate that within the alignment offset up to 0.5  $\mu\text{m}$ , the predicted insertion loss values remain relatively constant at near 27 dB and near 0 dB for both the bottom and the suspended waveguides, respectively. However, for alignment offsets beyond 0.6  $\mu\text{m}$ , the coupling efficiency is predicted to be compromised. The fluctuating trend in the bottom waveguide's insertion loss with respect to alignment offset is attributed to a combined effect of mode mismatch, evanescent coupling efficiency variations, and interference due to the tapered structure of the suspended waveguide.<sup>[63,64]</sup>

## 3. Fabrication

The full fabrication process of the switch is depicted in **Figure 4**. The process begins with an inductively coupled plasma (ICP)–

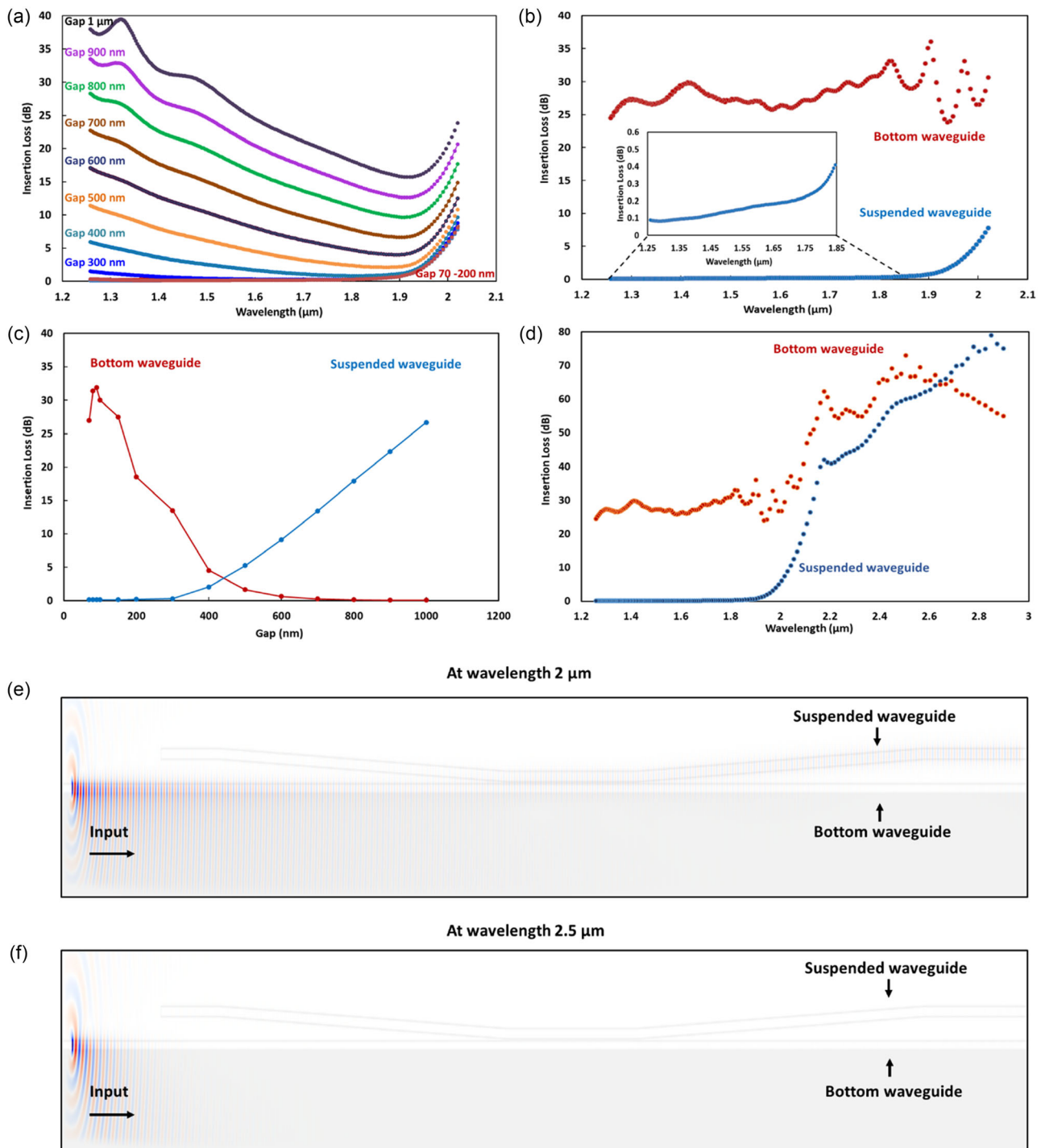


**Figure 2.** Numerical simulation of the SiNx switch. a) The insertion loss at the output of the suspended waveguide as a function of wavelength (1.2–2 μm) with increasing gap spacing between the waveguides, b) insertion loss as a function of wavelength for the bottom and suspended waveguides in the ON state of the switch, c) insertion loss as a function of gap for both waveguides of the switch at 1550 nm wavelength; d) insertion loss as a function of wavelength from 1.2 to 3 μm; FDTD simulations of the switch in the ON state at wavelengths e) 2 μm, and f) 2.5 μm.

CVD deposition of 4 μm thick SiO<sub>x</sub> on top of a Si wafer. Metal evaporation was used to create 70 nm thick bottom actuation electrodes, followed by a lift-off process (Step a). Subsequently, an ICP–CVD SiNx layer of 450 nm in thickness is deposited, and

ICP–reactive ion etching (RIE) patterned to form the bottom waveguide (Step b). The same thickness of SiNx material also covered the patterned bottom actuation electrodes. The conformal nature of the SiNx layer deposition process results in

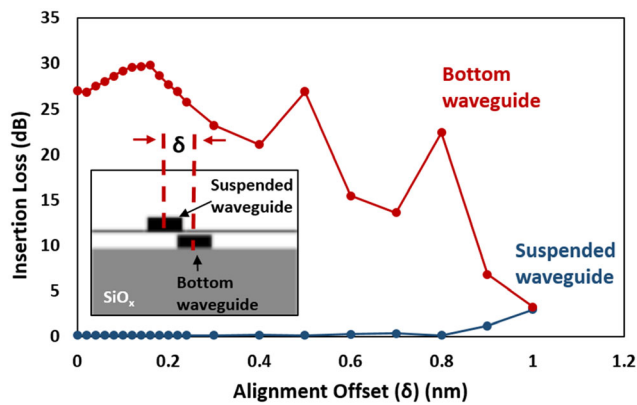


**Figure 3.** Insertion loss as a function of alignment offset ( $\delta$ ) between the bottom waveguide and the suspended waveguide. The inset shows the cross-sectional view of both waveguides along the YZ-plane, as defined in Figure 1. The blue and red data points are presented for the suspended waveguide and the bottom waveguide, respectively. The points are connected with a line to guide the eye.

70 nm raised regions, above the area of the bottom electrodes, which serve as mechanical stoppers for the device when actuated downward to the ON state. This method was developed to

prevent device failure issues caused by the lack of planarization of the top surface of the bottom waveguide layer. The devices were not planarized due to a lack of resources. The fabrication process illustrated in Figure 4 includes the planarization of the bottom waveguide layer; it has been designed in this manner for clarity (Step c). Next, a 1.1  $\mu\text{m}$  thick sacrificial layer of polyimide (PI2610) was applied and (Step d) the anchors were patterned by fully etching the polyimide (Step e). Further, a 450 nm thick  $\text{SiN}_x$  layer was deposited and patterned by using ICP-CVD to define the top suspended waveguide. After forming the top suspended waveguide by etching the 450 nm thick layer (Step f), another 100 nm thick  $\text{SiN}_x$  layer was added as an overcoat and extended beyond the coupler waveguide. This 100 nm thick  $\text{SiN}_x$  layer acted as the supporting membrane for the coupler waveguide as well as to aid in reducing the side-wall roughness of the top waveguide caused by the dry etching process (Step g). Subsequently, 70 nm thick top actuation electrodes were fabricated by thermal evaporation and a lift-off process (Step h). Finally, the sacrificial layer was etched using oxygen plasma in a plasma asher, thereby releasing the membrane layer and suspending the top waveguide. The ashing process is paused midway during the plasma etching stage, allowing the cleaving of the entire wafer and preparing the coupler devices for subsequent characterization through butt-coupling. Following this step, each subset of devices undergoes

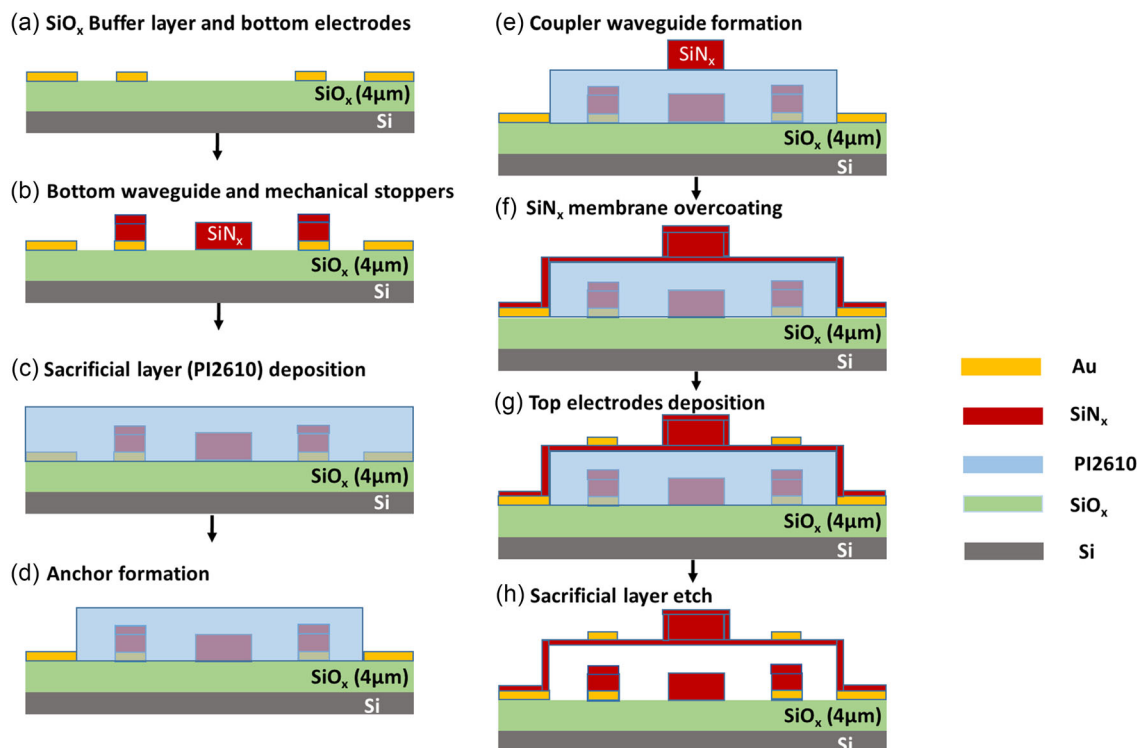


**Figure 4.** Fabrication process flow for MEMS  $\text{SiN}_x$  photonic switch. a) Deposition of a 4  $\mu\text{m}$   $\text{SiO}_x$  layer on Si substrate using ICP-CVD. Subsequently, a 70 nm layer of gold is patterned through thermal evaporation and lift-off processes to create the bottom electrodes. b) A 450 nm layer of  $\text{SiN}_x$  is deposited via ICP-CVD, followed by the patterning and etching of the bottom waveguide using ICP-RIE. c) Spinning of polyimide (PI2610) as a sacrificial layer of 1.1  $\mu\text{m}$  thickness. d) The sacrificial layer is patterned and etched to create anchors. e) A 450 nm layer of  $\text{SiN}_x$  is deposited via ICP-CVD, which is then patterned and etched to form the top coupler waveguide. f) A 90 nm layer of  $\text{SiN}_x$  is deposited to create the membrane. g) To prepare the top actuation electrodes, a 70 nm layer of gold is evaporated and followed by the lift-off process. h) The sacrificial layer is etched using oxygen plasma in an asher system.

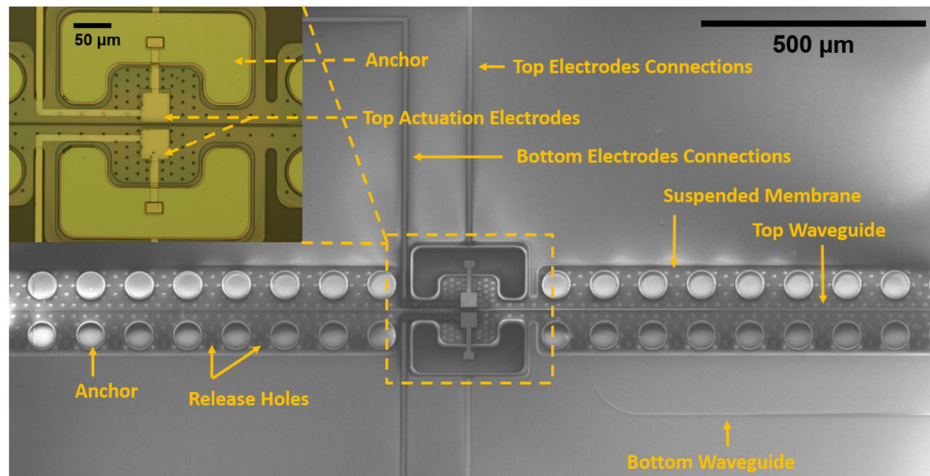


**Figure 5.** SEM image presenting a top view of the fabricated MEMS SiN<sub>x</sub> photonic switch, highlighting key components including the bottom waveguide, suspended waveguide, suspended membrane, anchors, gold connection lines, and release holes. A zoomed-in microscope image, at the top-left inset, offers a closer view of the switching area within the device.

additional exposure to oxygen plasma to complete the release process.

The top view of the fabricated device is depicted in **Figure 5** through a scanning electron microscopy (SEM) image. In this image, the bottom waveguide is built on the substrate and features an S-shaped bend leading toward the output. The suspended coupler waveguide is positioned above the suspended membrane, which is supported by anchors connected to the substrate. The SEM image also displays the gold connection lines for the top and bottom actuation electrodes. To provide a closer look at the switching area, a zoomed-in view is included as the top-left inset, revealing clear visualizations of the top actuation electrodes, anchors, and the release holes used for etching the sacrificial layer.

#### 4. Characterization Results and Discussion

Butt-coupling was used to launch light into the fabricated SiN<sub>x</sub> photonic switch devices. The set-up consisted of a pair of collimators ( $f = 11.29$  mm) and focusing lenses ( $f = 3.1$  mm) used to couple the laser into the input facet of the bottom waveguide and to collect the light from the output facets of the bottom and top waveguides. Two convex lenses were used to image the waveguides onto a visible camera ( $3280 \times 2464$  pixels). Initially, a red laser (650 nm) was used to align the laser spot at the input facet of the bottom waveguide. Subsequently, the red laser was replaced with an infrared laser of 1550 nm wavelength and a polarization controller (paddles) was used to optimize TE-polarized light into the device for maximum coupling efficiency. A tunable laser (1532–1575 nm) with a built-in detector (Agilent, Lightwave measurement system-8164B) was used for the short-wave optical measurements. A high-voltage amplifier (TEGAM, Model 2350) and a waveform generator (Agilent, 33210A) were used for electrostatic actuation of the top waveguide, allowing deflection toward the bottom waveguide to switch between the OFF and ON states of the coupler. The fabricated switch devices were prepared for electrostatic actuation characterization by

connecting to the samples using a gold wire bonding process. To measure the efficiency of the switch, butt-coupled TE-polarized light was launched into the input of the device allowing the outputs shown in Figure 1a,b to be measured. The input width of the bottom waveguide is tapered from 8 to 1.2  $\mu\text{m}$  to reduce the input coupling loss, while the output width of both waveguides is kept at 2  $\mu\text{m}$ . The input and output ports of the bottom waveguide are fixed to the substrate, while the output port of the suspended waveguide floats above the substrate. The measured characteristics of the device are shown in **Figure 6a,b**, illustrating two distinct sets of wavelengths: 1550 and 1470 nm, respectively. The measurements used an input laser power of 2.2 mW at a wavelength of 1550 nm, and 1.63 mW at 1470 nm. In Figure 6, the first row of columns (in the foreground) represents the OFF state of the coupler, where no voltage is applied to the electrodes and light is confined within the bottom waveguide. In this OFF state, the maximum measured output power from the bottom waveguide was 14  $\mu\text{W}$ , while the output light power from the suspended waveguide was only 4.6 nW. These results confirm that light propagation is confined to the bottom waveguide in the OFF state.

In contrast, the second row of columns (background) in Figure 6 represents the ON state, where the top suspended coupler waveguide is electromechanically pulled downward, allowing light to couple out of the bottom waveguide and propagate into the top waveguide. Upon applying a 50 volt DC voltage, the suspended waveguide was actuated downward toward the bottom waveguide, stopping at a 70 nm gap between the two waveguides. In this ON state at the output, the output light power from the bottom waveguide reduced to 1.4  $\mu\text{W}$ , while in the suspended waveguide, it increased to 11.8  $\mu\text{W}$ , confirming efficient coupling of light from the bottom waveguide to the suspended coupler waveguide. These measurements indicate an ON/OFF ER of 10 dB and 34 dB at the bottom substrate waveguide and at the top suspended waveguide, respectively. Similar observations were made for the 1470 nm wavelength (depicted in Figure 6b), showing a slightly higher ER of 17 dB at the bottom

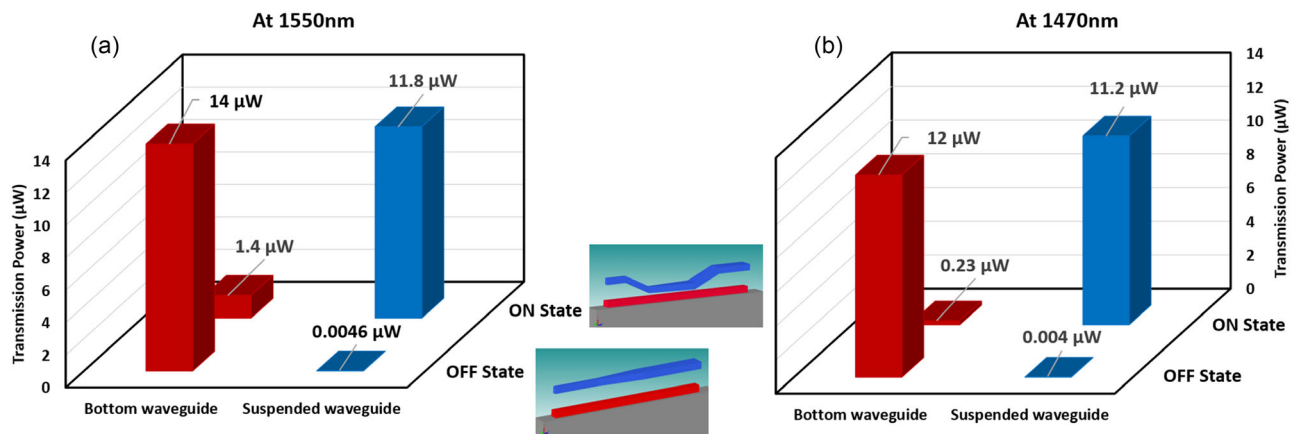


**Figure 6.** Measured optical transmission through the switching element: a) measurements at 1550 nm and b) measurements at 1470 nm. In the foreground, the first row of columns represents the OFF state of the switch, and the second row of columns represents the ON state. The measurements of light transmission at the outputs of the fixed bottom waveguide and the suspended coupler waveguide are depicted by red and blue colored columns, respectively.

substrate waveguide and the same 34 dB extinction at the top suspended waveguide.

In literature, “optical loss” describes the loss of input power during propagation that is no longer available for meaningful use. This can be shown by the waveguide’s propagation loss measured in dB/cm, or the insertion loss of a switch, which accounts for all losses from the input to any of its outputs. For the following discussion, we include the intended meaning of insertion loss to refer to path loss as the ratio of input to output powers along specified waveguide paths, either the switch bottom path or suspended path. The measured insertion loss as a function of wavelength (1.25–1.65  $\mu\text{m}$ ) is shown in **Figure 7**, obtained after subtracting the input and output coupling losses of 19 dB, estimated from the cut-back measurement method.<sup>[65]</sup> In the OFF state (Figure 7a) where the bottom and top waveguides are separated by a 1.1  $\mu\text{m}$  gap, the insertion loss from the bottom waveguide (shown in red) ranges from 2.3 to 4 dB while the suspended waveguide insertion loss (shown in blue) is  $42 \pm 3$  dB. In both cases, higher loss occurs in the shorter wavelength range. In the ON state, light is transmitted from the bottom waveguide to the suspended one, resulting in increased insertion loss in the bottom waveguide, as shown by the red circular points in Figure 7b. This loss is observed to vary between 10 and 23 dB over the wavelength range of 1.27–1.61  $\mu\text{m}$ . In contrast, the insertion loss of the suspended waveguide decreases between 2.6 and 5.5 dB within the same wavelength spectrum. These results confirm that the insertion loss from the suspended waveguide in the ON state is about the same as that in the OFF state from the bottom waveguide, indicating that the suspended waveguide and light switching do not contribute significantly to any additional loss. Within the suspended waveguide in the ON state, the insertion loss within the wavelength range of 1.27–1.61  $\mu\text{m}$  is characterized to have a variation of only  $2 \pm 1$  dB, which is largely attributed to waveguide propagation losses comprised of scattering and absorption losses.

The insertion loss as predicted by simulations using the MEEP software is included in Figure 7b for the bottom and suspended

waveguides, and shown using symbols connected by red and blue dashed lines, respectively. Over the indicated wavelength range, the modeled results show the ON state extinction in the bottom waveguide to be  $27.5 \pm 1.5$  dB, whereas maximum coupled light into the suspended waveguide in this state has an insertion loss value of only  $0.125 \pm 0.045$  dB. As our model did not take scattering losses into account, we believe the difference between the simulated and measured insertion loss values is largely due to fabrication imperfections and the nonplanarization of the bottom waveguide layer, which can be improved using chemical mechanical polishing.<sup>[44]</sup> The ERs for both waveguides at each presented wavelength are shown in a table included in Figure 7, where it can be observed that the bottom waveguide has a maximum ER of 17.75 dB at 1330 nm while the suspended waveguide maximum extinction of 42.18 dB occurs at 1410 nm. The alternating variation in the ER for the bottom waveguide is thought to be due to interaction with the silicon substrate.

As this is a dynamic MEMS-based switch, switching time was measured by applying a step voltage to the electrodes, as shown in **Figure 8**, to deflect the suspended membrane toward the substrate. The transmission was monitored at the bottom waveguide and hence the measured signal decreased when the coupler was actuated (ON state). The speed of transition between the switch ON and OFF state is shown in Figure 8, which indicates measured rise time (10–90% power) and fall time (90% to 10% power) of 10 and 35  $\mu\text{s}$ , respectively. These times are considerably faster than conventional 2D or 3D MEMS switches. By manipulating the properties of waveguides, light can be switched without the necessity of physically moving large mechanical structures. Consequently, the switching operation achieves faster speeds as it eliminates the mechanical displacement and settling times associated with 3D or 2D MEMS switches.<sup>[66,67]</sup> This measurement was performed on a different coupler device since the prior device (the device that was used to demonstrate the transmission levels, which is reported in Figure 6 and 7) was permanently pulled down and did not recover after being left in the ON

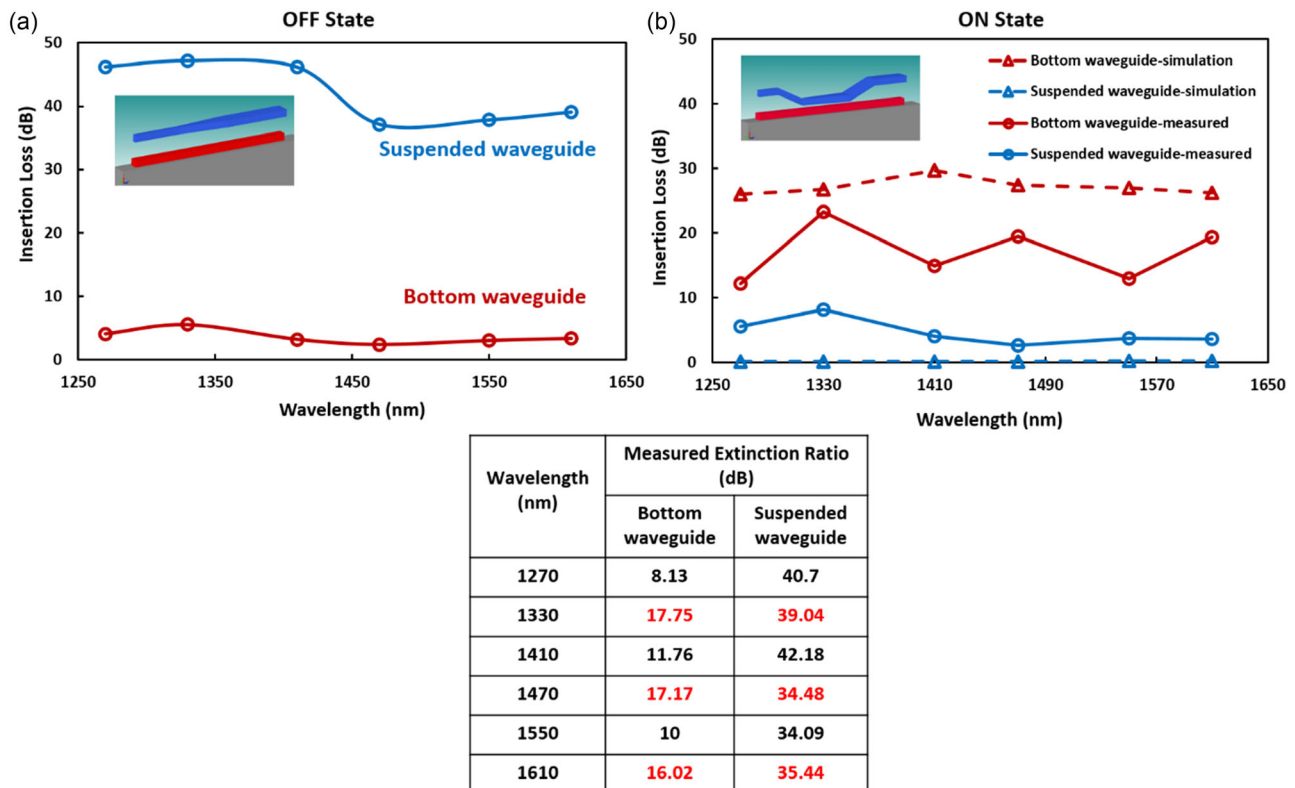


**Figure 7.** Wavelength dependence of the switch characterized by insertion loss measurements at the two outputs for a wide range of wavelengths (1250–1650 nm): measurements at the output of the bottom waveguide (red) and the suspended coupler waveguide (blue) are presented for both the a) OFF state and b) ON state. Measured data are presented as continuous lines and simulated data are presented as dotted lines for the ON state of the switch. The measured ERs for both the bottom and suspended waveguides are presented in the table.

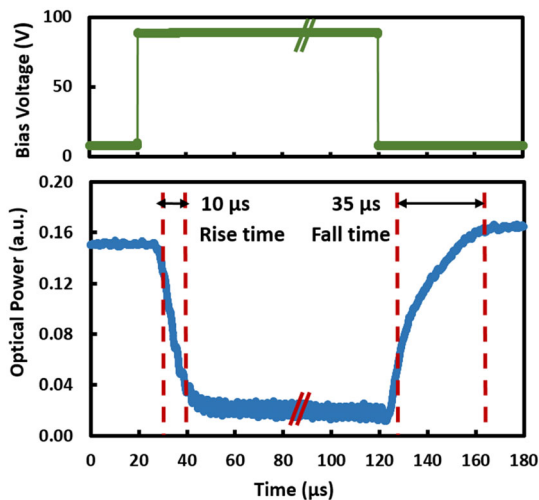


**Figure 8.** Optical power (blue line) in the bottom waveguide as a function of time measured with the application of bias voltage (green line). The rise and fall times of 10 and 35  $\mu$ s, respectively, relate to the light being switched from the bottom waveguide to the suspended waveguide.

state for an extended period of time. This might be due to the large mechanical stoppers, which increase the contact surface area when the device is in the ON state. This expanded contact

area can amplify the adhesive forces, making it more challenging for the device to recover from the ON state.<sup>[48]</sup>

To reduce the required 50 V actuation voltage, adjustments to the switch's mechanical design can be introduced. Increasing the area of the actuation electrodes and fine-tuning the stiffness parameters of the suspended structure can be used to reduce the actuation voltage. Optimization of the spring constant and stiffness of the suspended structure can provide the right balance between the actuation voltage and the structure's resonance frequency, enhancing the device's switching speed. Further, reducing the size of the mechanical stoppers can help in overcoming the stiction issues for the MEMS structures. The use of hermetic packaging can maintain switch performance and device stability by protecting it from environmental influences.<sup>[68]</sup> This was not part of the fabrication process used in this article with optimization of mechanical stability being beyond the scope of our work. However, it needs to be noted that common foundry processes include hermetic packaging and address device degradation. Adoption of DC for the actuation mechanisms and materials inhibiting any leakage currents would aid to ensure that once the switch is in its desired state, negligible power is consumed to maintain that state. The calculated capacitance of 9.5 F for our current actuator design confirms that minimal energy is required to charge or discharge the capacitor during the actuation process. A minimal resistance of 0.6 ohms calculated across the electrical contacts for the realized devices confirms that the power

dissipated due to resistive heating is relatively low, further enhancing energy efficiency.

## 5. Conclusion

This article has introduced a new design for a MEMS-based silicon nitride photonic switch that achieves excellent performance without requiring sub-100 nm resolution lithography. The photonic switch was successfully fabricated and tested, exhibiting an insertion loss of 2.6 and 3.7 dB at 1470 and 1550 nm wavelengths, respectively. The suspended waveguide achieved a high ER between the OFF and ON states of 34 dB at 1470 nm. The device achieves broadband operation across a wide range of 600 nm, from 1250 to 1850 nm, which is the widest range reported for a MEMS photonic switch to date. Furthermore, the measured rise time of the optical switch was within the 10  $\mu$ s range. To our knowledge, this is the first report of a MEMS photonic switch demonstrating adiabatic coupling that employs SiN<sub>x</sub> waveguides and vertical parallel plate actuation, allowing established microfabrication techniques to be used to create silicon-on-insulator high-performance optical waveguide switches.

## Acknowledgements

This work used the facilities of the Western Australian node of the NCRIS-enabled Australian National Fabrication Facility (ANFF) and support from the Western Australian Government's Department of Jobs, Tourism, Science and Innovation. This research was financially supported by the ARC (CE200100010), the Australian Government Research Training Program International Fees Scholarship, and a University Postgraduate Award. The authors also thankfully acknowledge the resources provided by the Pawsey Supercomputing Centre, and the facilities of the Centre for Microscopy, Characterisation & Analysis (CMCA) at The University of Western Australia.

Open access publishing facilitated by The University of Western Australia, as part of the Wiley - The University of Western Australia agreement via the Council of Australian University Librarians.

## Conflict of Interest

The authors declare no conflict of interest.

## Data Availability Statement

The data that support the findings of this study are available from the corresponding author upon reasonable request.

## Keywords

adiabatic coupling, fabrication, finite difference time domain, microelectromechanical systems, optical simulations, photonic switches, silicon nitride waveguide

Received: July 14, 2023  
Revised: October 15, 2023  
Published online:

- [1] D. Nicolas, B. G. Lee, A. V. Rylakov, D. M. Kuchta, C. W. Baks, J. S. Orcutt, D. M. Gill, W. M. J. Green, C. L. Schow, *J. Lightwave Technol.* **2015**, 33, 3597.
- [2] Z. Lu, D. Celo, H. Mehrvar, E. Bernier, L. Chrostowski, *Sci. Rep.* **2017**, 7, 12244.
- [3] L. Schares, T. N. Huynh, M. G. Wood, R. Budd, F. Doany, D. Kuchta, N. Dupuis, B. G. Lee, C. L. Schow, M. Moehle, in *Optical Fiber Communication Conf.*, Anaheim, CA **2016**, p. Th3F-5.
- [4] L. Fan, S. Gloeckner, P. D. Dobbelaere, S. Patra, D. Reiley, C. King, T. Yeh, J. Gritters, S. Gutierrez, Y. Loke, in *Optical Fiber Communication Conf. Exhibit*, Anaheim, CA **2002**, p. TuO4.
- [5] N. T. Tsutomu Kitoh, K. Jingui, M. Yasu, M. Kawachi, *IEEE Photonics Technol. Lett.* **1992**, 4, 735.
- [6] Q. Cheng, A. Wonfor, J. L. Wei, R. V. Penty, I. H. White, in *Optical Fiber Communication Conf.*, Los Angeles, CA **2015**, p. Th4E-6.
- [7] A. d'Alessandro, R. Asquini, *Mol. Cryst. Liq. Cryst.* **2003**, 398, 207.
- [8] X. Ma, G.-S. Kuo, *IEEE Commun. Mag.* **2003**, 41, S16.
- [9] M. Mendez-Astudillo, M. Okamoto, Y. Ito, T. Kita, *Opt. Express* **2019**, 27, 899.
- [10] H. R. Mojaver, V. Tolstikhin, B. Gargallo, R. Baños, D. Domenech, J. Lo, D. Kumar, K.-W. Leong, O. Liboiron-Ladouceur, *Opt. Letters* **2020**, 45, 4650.
- [11] L. W. Shacklette, P. M. Ferm, R. Blomquist, K. M. Killian, L. Guiziou, L. S. H. K. Chun, J. M. Jouanno, *SPIE Proc.* **2002**, 4642, 1.
- [12] T.-W. Yeow, K. L. E. Law, A. Goldenberg, *IEEE Commun. Mag.* **2001**, 39, 158.
- [13] C. Wu, H. Yu, H. Li, X. Zhang, I. Takeuchi, M. Li, *ACS Photonics* **2018**, 6, 87.
- [14] M. Yano, F. Yamagishi, T. Tsuda, *IEEE J. Sel. Top. Quantum Electron.* **2005**, 11, 383.
- [15] T. J. Seok, J. Luo, Z. Huang, K. Kwon, J. Henriksson, J. Jacobs, L. Ochikubo, R. S. Muller, M. C. Wu, *APL Photonics* **2019**, 4, 42306.
- [16] L. Qiao, W. Tang, T. Chu, *Sci. Rep.* **2017**, 7, 42306.
- [17] L. Lu, S. Zhao, L. Zhou, D. Li, Z. Li, M. Wang, X. Li, J. Chen, *Opt. Express* **2016**, 24, 9295.
- [18] Q. Cheng, R. Stabile, A. Rohit, A. Wonfor, R. V. Penty, I. H. White, K. A. Williams, *J. Opt. Commun. Networking* **2015**, 7, A388.
- [19] Q. Cheng, R. Stabile, A. Rohit, A. Wonfor, R. V. Penty, I. H. White, K. A. Williams, in *Optical Fiber Communication Conf.*, San Francisco, CA **2014**, p. M3E-2.
- [20] R. Zhang, Y. He, Y. Zhang, S. An, Q. Zhu, X. Li, Y. Su, *Nanophotonics* **2020**, 10, 937.
- [21] Y. Yuan, J. Xie, Y. Ma, D. Luo, F. Fan, S. Wen, *Opt. Lett.* **2022**, 47, 957.
- [22] X.-B. Wang, J. Sun, Y.-F. Liu, J.-W. Sun, C.-M. Chen, X.-Q. Sun, F. Wang, D.-M. Zhang, *Opt. Express* **2014**, 22, 11119.
- [23] T. Sutili, P. Rocha, C. M. Gallep, E. Conforti, *J. Lightwave Technol.* **2019**, 37, 6015.
- [24] M. Murakami, *J. Networks* **2010**, 5, 1254.
- [25] L. Medina, R. Gilat, S. Krylov, *Int. J. Eng. Sci.* **2018**, 130, 75.
- [26] S. Kitamura, K. Komatsu, M. Kitamura, in *Optical Amplifiers and Their Applications*, Breckenridge, CO **1994**, p. WD2.
- [27] L. Almeida, R. Ramadoss, R. Jackson, K. Ishikawa, Q. Yu, *J. Micro/Nanolithogr., MEMS, MOEMS* **2007**, 6, 023009.
- [28] A. M. Al-Hetar, A. B. Mohammad, A. S. M. Supa'at, Z. A. Shamsan, *J. Lightwave Technol.* **2010**, 29, 171.
- [29] L. Chen, Y.-K. Chen, *Opt. Express* **2012**, 20, 18977.
- [30] B. G. Lee, A. V. Rylakov, W. M. Green, S. Assefa, C. W. Baks, R. Rimolo-Donadio, D. M. Kuchta, M. H. Khater, T. Barwicz, C. Reinholm, E. Kiewra, *J. Lightwave Technol.* **2014**, 32, 743.
- [31] J. W. Silverstone, D. Bonneau, J. L. O'Brien, M. G. Thompson, *IEEE J. Sel. Top. Quantum Electron.* **2016**, 22, 390.
- [32] G. Son, S. Han, J. Park, K. Kwon, K. Yu, *Nanophotonics* **2018**, 7, 1845.

- [33] R. Marchetti, C. Lacava, L. Carroll, K. Gradkowski, P. Minzioni, *Photonics Res.* **2019**, 7, 201.
- [34] X. Chen, J. Lin, K. Wang, *Laser Photonics Rev.* **2023**, 17, 2200571.
- [35] C. Errando-Herranz, A. Y. Takabayashi, P. Edinger, H. Sattari, K. B. Gylfason, N. Quack, *IEEE J. Sel. Top. Quantum Electron.* **2020**, 26, 8200916.
- [36] Q. Fang, J. F. Song, T.-Y. Liow, H. Cai, M. B. Yu, G. Q. Lo, D.-L. Kwong, *IEEE Photonics Technol. Lett.* **2011**, 23, 525.
- [37] P. Sun, R. M. Reano, *Opt. Express* **2010**, 18, 8406.
- [38] R. Soref, B. Bennett, *IEEE J. Quantum Electron.* **1987**, 23, 123.
- [39] L. Lu, X. Li, W. Gao, X. Li, L. Zhou, J. Chen, *IEEE Photonics J.* **2019**, 11, 6603209.
- [40] E. Bulgan, Y. Kanamori, K. Hane, *Appl. Phys. Lett.* **2008**, 92, 101110.
- [41] M. D. L. Franck Chollet, H. Fujita, *IEEE J. Sel. Top. Quantum Electron.* **1999**, 5, 52.
- [42] E. Ollier, *IEEE J. Sel. Top. Quantum Electron.* **2002**, 8, 155.
- [43] J. Yao, D. Leuenberger, M.-C. M. Lee, M. C. Wu, *IEEE J. Sel. Top. Quantum Electron.* **2007**, 13, 202.
- [44] T. J. S. S. Han, N. Quack, B.-W. Yoo, M. C. Wu, *Optica* **2015**, 2, 370.
- [45] Y. K. Yuta Akihama, K. Hane, *Opt. Express* **2011**, 2011, 23658.
- [46] Y. Akihama, K. Hane, *Light: Sci. Appl.* **2012**, 1, e16.
- [47] S. Abe, K. Hane, *IEEE Photonics Technol. Lett.* **2013**, 25, 675.
- [48] N. Q. T. J. Seok, S. Han, R. S. Muller, M. C. Wu, *Optica* **2016**, 3, 64.
- [49] K. K. Tae Joon Seok, J. Henriksson, J. Luo, M. C. Wu, *Optica* **2019**, 6, 490.
- [50] S. Sharma, N. Kohli, J. Briere, F. Nabki, M. Menard, *Opt. Express* **2022**, 30, 22200.
- [51] G. N. Nielson, D. Seneviratne, F. Lopez-Royo, P. T. Rakich, Y. Avrahami, M. R. Watts, H. A. Haus, H. L. Tuller, G. Barbastathis, *IEEE Photonics Technol. Lett.* **2005**, 17, 1190.
- [52] C. Pinho, F. Rodrigues, A. M. Tavares, C. Rodrigues, C. E. Rodrigues, A. Teixeira, *Appl. Sci.* **2020**, 10, 4024.
- [53] X. Sun, J. Feng, L. Zhong, H. Lu, W. Han, F. Zhang, R. Akimoto, H. Zeng, *Opt. Laser Technol.* **2019**, 119, 105641.
- [54] S. Xie, S. Veilleux, M. Dagenais, *IEEE Photonics J.* **2022**, 14, 2237906.
- [55] R. Sun, M. Beals, A. Pomerene, J. Cheng, C.-Y. Hong, L. Kimerling, J. Michel, *Opt. Express* **2008**, 16, 11682.
- [56] P. K. J. Singaravelu, G. C. R. Devarapu, S. A. Schulz, Q. Wilmart, S. Malhouitre, S. Olivier, *J. Phys. D: Appl. Phys.* **2019**, 52, 214001.
- [57] P. J. Withers, H. Bhadeshia, *Mater. Sci. Technol.* **2001**, 17, 355.
- [58] M. Martyniuk, J. Antoszewski, C. Musca, J. Dell, L. Faraone, *Smart Mater. Struct.* **2005**, 15, S29.
- [59] S. Dutta, A. Pandey, *J. Mater. Sci.: Mater. Electron.* **2021**, 32, 6705.
- [60] M. Martyniuk, J. Antoszewski, C. Musca, J. Dell, L. Faraone, *J. Appl. Phys.* **2006**, 99, 053519.
- [61] M. Martyniuk, C. Musca, J. Dell, L. Faraone, *Mater. Sci. Eng., B* **2009**, 163, 26.
- [62] B. Walmsley, Y. Liu, X. Hu, M. Bush, K. Winchester, M. Martyniuk, J. Dell, L. Faraone, *J. Appl. Phys.* **2005**, 98, 044904.
- [63] K. Okamoto, *Fundamentals of Optical Waveguides*, Elsevier, San Diego, CA **2021**.
- [64] G. T. Reed, A. P. Knights, *Silicon Photonics: An Introduction*, John Wiley & Sons, Chichester, West Sussex, England **2004**.
- [65] R. G. Hunsperger, *Integrated Optics: Theory and Technology*, Springer Science & Business Media, New York, NY **2009**.
- [66] H. Toshiyoshi, H. Fujita, *J. Microelectromech. Syst.* **1996**, 5, 231.
- [67] Q. Cheng, S. Rumley, M. Bahadori, K. Bergman, *Opt. Express* **2018**, 26, 16022.
- [68] W. A. de Groot, J. R. Webster, D. Felnhof, E. P. Gusev, *IEEE Trans. Device Mater. Reliab.* **2009**, 9, 190.